Applied Catalysis B: Environmental 176–177 (2015) 150–159

Contents lists available at ScienceDirect

Applied Catalysis B: Environmental

journal homepage: www.elsevier.com/locate/apcatb

Thermally induced changes in the structure and ethanol oxidation activity of $Pt_{0.25}Mn_{0.75}/C$

M.R. Zamanzad Ghavidel, E. Bradley Easton*

Faculty of Science, University of Ontario Institute of Technology, 2000 Simcoe Street North, Oshawa, Ontario L1H 7K4, Canada

ARTICLE INFO

Article history:
Received 3 November 2014
Received in revised form 16 March 2015
Accepted 29 March 2015
Available online 31 March 2015

Keywords:
Pt–Mn alloy
Heat treatment
Ethanol oxidation
Catalysts
PEM fuel cell
Direct alcohol fuel cells

ABSTRACT

Decreasing the cost associated with platinum based catalysts along with improving catalytic properties is a major challenge for commercial direct alcohol fuel cells (DAFC). In this work, Pt/C and Pt–Mn/C alloys have been synthesized and the impact of heat treatment on the structure and electrochemical properties of these catalysts was investigated. The structure, composition and thermal properties of the samples were studied by X-ray diffraction (XRD), X-ray photoelectron spectroscopy (XPS) and thermogravimetric analysis (TGA). TGA and XRD data showed the Pt–Mn deposits did not have a uniform structure. Several phase transitions occurred upon heat treatment of the catalysts at temperatures between 500 and 950 °C. Cyclic and linear sweep voltammetry illustrated that the ethanol oxidation reaction (EOR) activity of pure Pt and Pt–Mn alloy catalysts was altered significantly by heat treatment. The highest EOR activity was achieved with a Pt–Mn alloy that was annealed at 700 °C for 4 h, exceeding the EOR activity of the pure Pt and untreated Pt–Mn alloy catalysts. XRD analysis indicated that at 700 °C an ordered PtMn intermetallic phase was formed and that these highly alloyed particles were the reasons for the enhanced EOR activity.

1. Introduction

In the last few decades, significant research efforts have focused on the reduction of the costs associated with direct alcohol fuel cells (DAFCs) [1–5]. The cost and lifetime of the DAFCs are mainly controlled by the catalysts used at each electrode. Pt is the most commonly utilized electrocatalyst. In order to decrease the cost and increase the lifetime of the DAFCs, it is essential to lower the required loading of Pt. In general, there are two methods to enhance the performance of a catalyst; first, by increasing the real surface area in contact with the reactant, which can be achieved by reducing particle size and improving particle dispersion; second, by enhancing the fundamental catalytic activity through the production of new materials or alloys [3,6].

There have been numerous studies of Pt-transition alloys for anodic fuel cell reactions, including Pt–Cu, Pt–Mo, Pt–Ni, Pt–Fe, Pt–Co, Pt–Sn and Pt–Ru [3,4,7–12]. It has been shown that Pt–Ru has the highest activity towards the methanol oxidation reaction (MOR) [7,13–17]. Conversely, Pt–Sn is has been shown to be more active than Pt–Ru towards the ethanol oxidation reaction (EOR), with the most active phase believed to be Pt_3Sn [13,15,16,18,19].

Our group has recently reported Pt–Mn alloys with high EOR activity [9,10]. Furthermore, the most active alloys contained less than 25 at% Pt, which is beneficial from a cost standpoint. Alloy formation was confirmed with XRD analysis. Those results showed that the presence of Mn affects both particle size and the intrinsic activity of the catalysts. However, the catalysts contained a mixture of weakly alloyed Pt–Mn and in-active oxide phases, which represents a limiting factor for performance.

Heat treatment has been recognized as an important and sometimes necessary step for catalytic activity improvement [5,20,21]. Heat treatment often leads to the removal of undesirable impurities present in the initial preparation (such as oxide phases). Furthermore, it can also lead to the formation of more uniform alloy particles with increased stability. This can often lead to an enhancement of catalytic performance, but not always. For example, heat treatment of Pt supported catalysts, even at low temperatures, leads to Pt particle growth via sintering. Sintering occurs via the migration and coalescence of the platinum particles or by evaporation and condensation of the atoms from small crystallites [21]. Therefore, the use of a heat treatment process can be detrimental, particularly for high purity single-element nanoparticle catalysts. However, the benefits of thermally treating alloy nanoparticles often outweigh any activity losses that may occur due to particle size growth. Optimization of the synthesis and heat treatment

* Corresponding author. Tel.: +1 905 721 8668x2936; fax: +1 905 721 3304.
E-mail address: Brad.Easton@uoit.ca (E.B. Easton).

http://dx.doi.org/10.1016/j.apcatb.2015.03.051
0926-3373/

process is often complex, and careful study is required in order to fully understand the reason for enhanced activity [4,5,21].

As with pure platinum particles, the grain sizes of the alloy particles can become enlarged at higher heat treatment temperatures. However, alloy catalysts often exhibit a better resistance to sintering than pure catalysts [21]. During heat treatment, the Pt lattice parameter and degree of alloying can be altered, and intermetallic and ordered phases can be formed depending upon the alloying element and the heat treating temperature [4,21,22]. Increasing the degree of alloying can lead to enhanced electrocatalytic activity because of electronic changes brought about by the presence of the alloying elements and changes in the inter-atomic Pt–Pt distance [17,21]. Furthermore, the heat treatment of alloy catalysts can potentially weaken [23] or improve [11] their durability and stability.

In this paper, we have studied the effects of heat treatment temperature and heating time on the crystalline structure and uniformity of Pt–Mn alloy phases. Additionally, the influence of heat treatment on particle size, catalyst dispersion and electrochemical surface area (ECSA) was examined. This structural information was correlated with EOR activity to determine the most active phases.

2. Experimental

2.1. Catalyst synthesis

Pt–Mn/C catalysts with a composition of $Pt_{0.25}Mn_{0.75}$ were synthesized by an impregnation method similar to our previous reports [24]. One equivalent of $H_2PtCl_6{\cdot}H_2O$ (Aldrich) and three equivalents of $MnCl_2{\cdot}4H_2O$ (Aldrich) were dissolved in deionized water. To this mixture, sufficient mass of Vulcan XC72R carbon black (Cabot Corp.) was added so that the final product had a total metal content of 20 wt%. This mixture was sonicated for 20 min. The pH of the solution was controlled and adjusted to 3 using HCl (15 v/v%), after which $NaBH_4$ was added in solid form to the mixture in a weight ratio of 3:1 to the metals. The final mixture was left overnight under constant stirring at room temperature. The powder was collected by suction filtration, washed with isopropanol alcohol (IPA), acetone, and deionized water, and finally dried in an oven at 80 °C overnight. For comparison, a control sample of 20 wt% Pt on carbon was prepared via the same synthetic procedure, which is hereafter referred to as Pt 100%.

A Barnstead Thermolyne tube furnace with a quartz tube was used for heat treating the samples. Heat treatment was performed in a nitrogen atmosphere at 500, 700, 875 and 950 °C for Pt–Mn/C samples and at 500 °C and 900 °C for the Pt/C samples. The period of heat treatment was kept constant (1 h) for all samples and temperatures, unless otherwise specified. After the heat treatment, the samples were cooled to room temperature under a constant flow of nitrogen.

2.2. Materials characterization

The Pt/Mn molar ratio in each sample was determined using a Varian Vista-MPX Inductively Coupled Plasma Optical Emission Spectroscopy (ICP-OES) system. Approximately 10 mg of the catalyst was dispersed in an Aqua Regia solution and left to dissolve for at least two days. Afterwards, the residue was filtered and the mother liquor was diluted and used for ICP-OES analysis. Four standard solutions of Pt and Mn with a concentration of 1, 5, 10 and 20 ppm were used for calibration.

X-ray photoelectron spectroscopy (XPS) was conducted using a Kratos Axis Ultra spectrometer equipped with a monochromatic Al Kα source (15 mA, 14 kV). The instrument work function was calibrated to give a binding energy (BE) of 83.96 eV for the Au $4f_{7/2}$ line of metallic gold and the spectrometer dispersion was adjusted so that the position of the Cu $2p_{3/2}$ line for metallic copper was 932.62 eV. The Kratos charge neutralizer system was used on all specimens. Spectra were charge corrected so that the main line for the carbon 1s spectrum (adventitious carbon) set to 284.8 eV. Spectra were analysed using CasaXPS software (version 2.3.14).

Powder X-ray diffraction (XRD) patterns were obtained using a Bruker D8 Advance powder X-ray diffractometer, with germanium monochromator and Cu Kα1 radiation. Thermogravimetric Analysis (TGA) and differential scanning calorimetry (DSC) were utilized to study phase transition versus temperature for the catalyst powder and to determine carbon/metal weight ratio. In addition, to study the effect of the heat treatment time on the phase transformations, cyclic thermal analysis (CTA) was utilized. The CTA provides the opportunity to analyze the same sample several times by defined cycles and to study fast (instantaneous) and slow phase transformations. Thermal analysis was performed using a TA Instruments Q600 SDT system. Measurements were made in both argon and air atmospheres, using a heating ramp of 5 °C/min and 20 °C/min, respectively.

Transmission Electron Microscopy (TEM) images were acquired using a Philips CM 10 instrument equipped with an AMT digital camera system. Samples for TEM analysis were dispersed in a mixture of water and isopropanol (IPA) and applied to nickel 400 mesh reinforced grids coated with carbon and allowed to dry under air before being introduced into the chamber.

2.3. Electrochemical characterization

To study the electrochemical activity of the samples, an electrode ink for each catalyst was prepared and used to deposit catalyst layers on glassy carbon (GC) electrodes. The inks were produced by mixing 10 mg of catalyst with 100 μL of Nafion solution (5% in alcohols, DuPont) and 400 μL of a 50:50 mixture of IPA and water. The mixture was sonicated for 45 min to achieve a uniform suspension. A 2 μL droplet of the well-dispersed catalyst ink was deposited onto a clean and polished glassy carbon electrode (diam = 3 mm, CH instruments), using a micro syringe, such that it covered the entire surface of the glassy carbon. The ink droplet was allowed to air dry at room temperature prior to electrochemical tests. The resultant catalyst layer had a total metal loading of 0.11 mg/cm^2. All electrochemical tests, such as cyclic voltammetry (CV) and linear sweep voltammetry (LSV), were conducted using a Solartron 1470 potentiostat. Measurements were made in N_2-purged 0.5 M H_2SO_4 (aq) electrolyte to determine the electrochemical active surface area (ESCA). EOR activity was assessed in a N_2-purged aqueous solution containing both 0.5 M H_2SO_4 + 0.1 M ethanol.

Table 1
Composition of the samples and concentration of Pt and Mn in filtrated solution which was measured by ICP.

Sample	Alloy molar ratios measured by ICP		Ions concentration in filtered solution by ICP		Metal loading wt%
	Pt (%)	Mn (%)	Pt (ppm)	Mn(ppm)	
Pt 100%	100	0	–	–	25.27
$Pt_{0.25}Mn_{0.75}$	22.18	77.82	Nil	Nil	22.75
Mn 100%	0	100	–	–	16.19

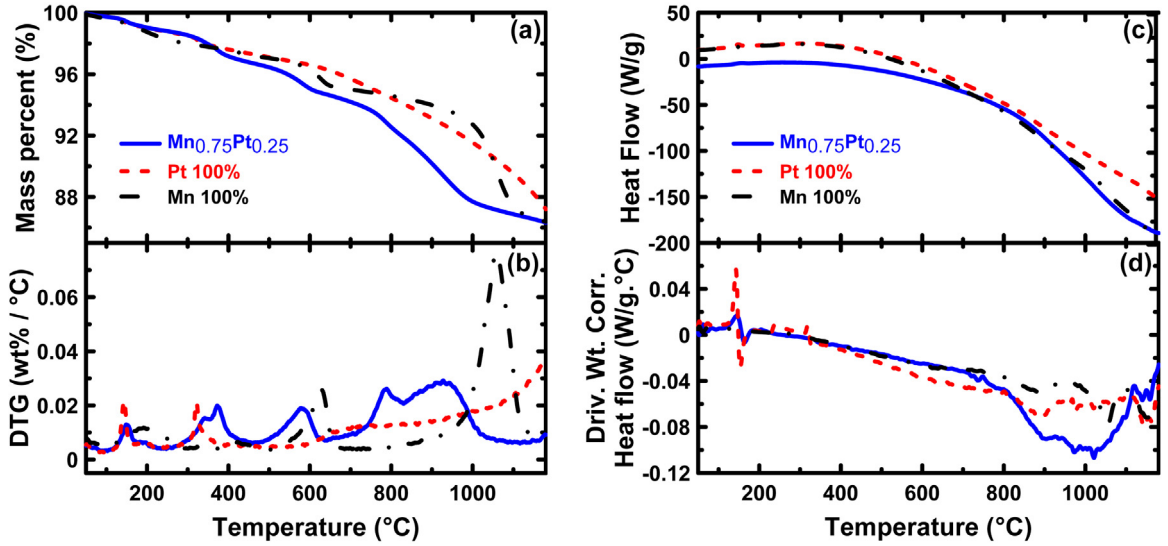

Fig. 1. (a) The weight loss and (b) derivative weight loss (c) heat flow and (d) derivative heat flow versus temperature for Pt, Mn and Pt–Mn alloys deposited on a Vulcan carbon support. Measurements were made at a heating rate of 5 °C/min under flowing argon.

3. Results and discussion

3.1. Materials characterization

The chemical composition of the samples and the residual solutions after chemical reduction were determined by ICP-OES and presented in Table 1. The ICP-OES tests showed that the Pt–Mn alloys were produced with a composition of 22 at% Pt and 78 at% Mn, quite close to the expected composition values ($Pt_{0.25}Mn_{0.75}$). The amount of Pt and Mn ions in the filtrate was also zero, indicating that nearly all of the metal ions were successfully reduced. TGA analysis performed under air indicated that the metal loading for all Pt/C and Pt–Mn/C samples were close to the expected 20 wt% metal. The metal loading was ca. 16 wt% for pure Mn sample (Table 1).

Fig. 1a and b shows the thermogravimetry (TG) and derivative thermogravimetry (DTG) curves obtained for the carbon supported pure Pt, pure Mn and Pt–Mn alloy catalysts. Five distinctive mass loss regions were observed. The mass loss occurring between 100 °C and 250 °C was attributed to the thermal decomposition of functional groups on carbon and the evaporation of any residual water in the samples [25,26]. A second major mass loss was observed around 300 °C, which was attributed to the oxidation of the carbon support by oxygen or the air trapped within the powdered samples [26]. The mass loss observed around 700 °C was attributed to loss of functional groups on carbon and its graphitization [25]. The mass losses observed at ca. 500 and 900 °C were attributed to Mn oxide phase modifications. Baturina et al. have shown that pure MnO_2 is reduced to Mn_2O_3 at 500 °C, and further reduced to Mn_3O_4 at 900 °C [27]. However, at room temperature, a mixture of these oxides is most likely present. Mn oxide transitions occurred at lower temperatures for the Pt–Mn/C alloy sample compared to the Mn/C samples, which indicates that Pt may help facilitate these transformations.

The DSC curves obtained for the pure and alloyed samples are illustrated in Fig. 1c and d. Most of the observed transitions were endothermic except those related to carbon combustion between 300 and 400 °C. The measured heat flow between 700 and 1000 °C for the Pt–Mn alloy (20.21 W/g) was higher than that measured for the pure Mn (12.04 W/g) and Pt (16.99 W/g) samples. This indicates that the alloy phase transformation began around 700 °C and completed at higher temperatures.

The cyclic weight loss, cyclic derivative weight loss and cyclic heat flows versus temperature are shown for the Pt–Mn alloy in Fig. 2. All phase transformations that occur below 700 °C were completed during the first cycle as there was no major mass loss in the second cycle in the same range (Fig. 2b). However, mass changes were observed at temperatures above 700 °C during the second cycle. The endothermic processes that occurred during the second cycle were most likely related to the alloying process and

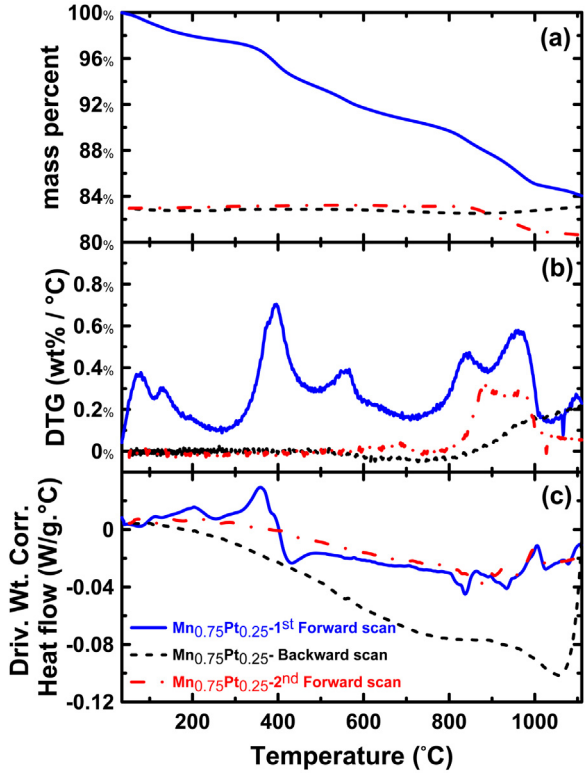

Fig. 2. The cyclic weight loss, derivative weight loss and derivative heat flow versus temperature in argon atmosphere for Pt–Mn alloys deposited on a Vulcan carbon support. Measurements were made at a heating rate of 20 °C/min under flowing argon.

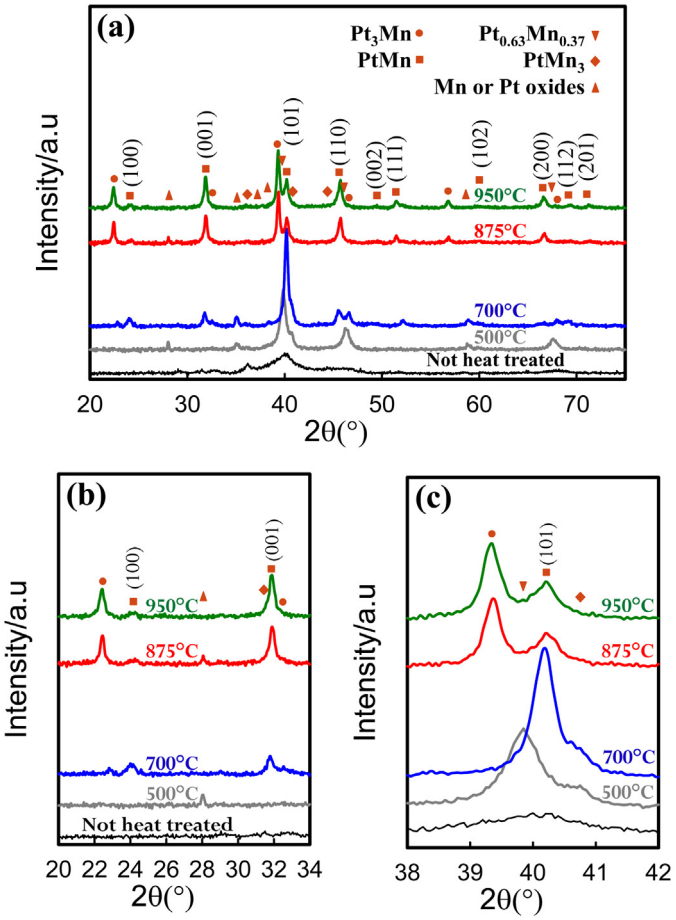

Fig. 3. XRD analysis of the Pt–Mn alloys before and after heat treatment in nitrogen atmosphere for constant period (1 h) at different temperatures.

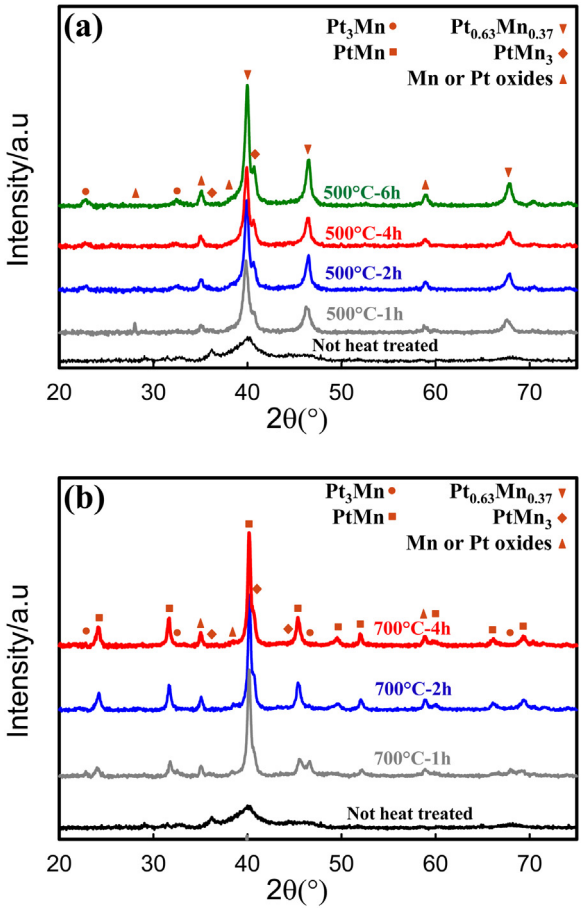

Fig. 4. XRD analysis of the Pt–Mn alloys before and after heat treatment for different periods at (a) 500 °C and (b) 700 °C in nitrogen atmosphere.

oxide removal at the higher temperature, indicating that these processes were somewhat slow (Fig. 2c). Therefore, the influence of heat treatment time on the structure and EOR activity of the samples was investigated in more detail. Based on the DSC results, heat treatment temperatures of 500, 700, 875 and 950 °C were selected for the Pt–Mn alloys catalysts, and at 500 and 900 °C for the pure Pt samples. In addition, the hold time at these heat treatment temperatures was also examined.

The XRD patterns obtained for samples heat treated at different temperatures for 1 h are shown in Fig. 3. Broad peaks were obtained for the untreated samples, indicating that the catalysts were produced with small grain sizes. The broadening of the peaks could also be due to the presence of oxide phases and non-uniform alloy. The diffractogram displayed the characteristics pattern expected for the face centered cubic (fcc) structure of Pt. The peak positions were shifted to higher angles, indicating the incorporation of Mn in the fcc Pt structure. Additionally, there was a peak observed at 36.2° which was likely related to Mn rich phases. Because of the extremely broad peaks, it was very difficult to precisely identify which alloy phases were formed during the chemical reduction. However, we can reasonably infer that the as-deposited catalysts contained a mixture of Pt–Mn alloys and other non-alloyed phases.

Heat treatment was employed to induce structural changes in the catalyst. Upon heat treatment at 500 °C, the reflections associated with the Mn rich phases in the XRD pattern disappeared. Furthermore, the intensity of the remaining peaks increased, indicating that crystallization and some structural changes were initiated at this temperature, although the predominant structure was still the Pt fcc structure. At this temperature, there were two kinds of distinctive phases: one rich in Mn and the other rich in Pt.

When the heat treatment temperature was raised to 700 °C, substantial changes in the intensity and position of several peaks were observed, particularly the (1 0 1) and (1 1 0) reflections. Moreover, new peaks appeared at lower diffraction angles (22–40°). All of these observations indicate that an ordered intermetallic phase was formed at 700 °C, which we have assigned to an intermetallic PtMn phase (ICDD card no. 01-071-9672). The important peaks are shown in expanded scales in Fig. 3b and c. The PtMn intermetallic phase has a tetragonal structure [4]; therefore, the new (1 0 0) and (0 0 1) peaks were observed at the lower diffraction angles of ~24.1° and ~31.7°, respectively. In addition, upon raising the heat treatment temperature, the peak observed at 39.8° for the sample heat treated at 500 °C shifted to 40.2° when the sample was heat treated at 700 °C, which was a result of further Pt and Mn alloying and intermetallic phase formation. In other words, at 700 °C a uniform alloy with a high alloying degree was generated, with PtMn as the predominant phase.

Upon further increasing the heat treatment temperature to 875 °C and 950 °C, additional peaks at ~22.4° and ~39.4° were observed, which were attributed to variation in the crystalline structure of the Pt–Mn intermetallic phases. The new peaks were most likely due to phase separation and the formation of phases with higher Pt content such as Pt_3Mn (see Fig. 3b). The origins of the phase separation warrants further investigation, but we postulate that particles or phases with a lower Mn content have been combined with the PtMn phase and formed Pt_3Mn like structures.

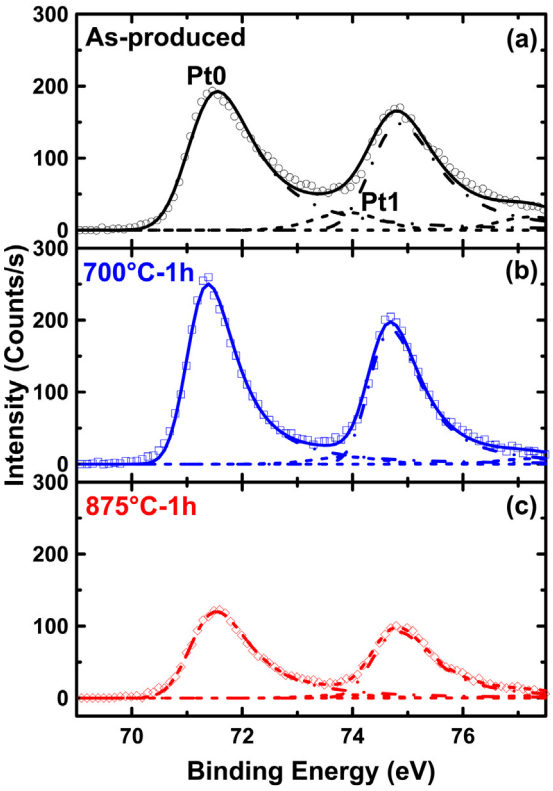

Fig. 5. XPS spectra of Pt 4f for the $Pt_{0.25}Mn_{0.75}$ alloy deposited on Vulcan carbon (a) As-produced and heat treated at (b) 700 °C and (c) 875 °C for 1 h in nitrogen atmosphere.

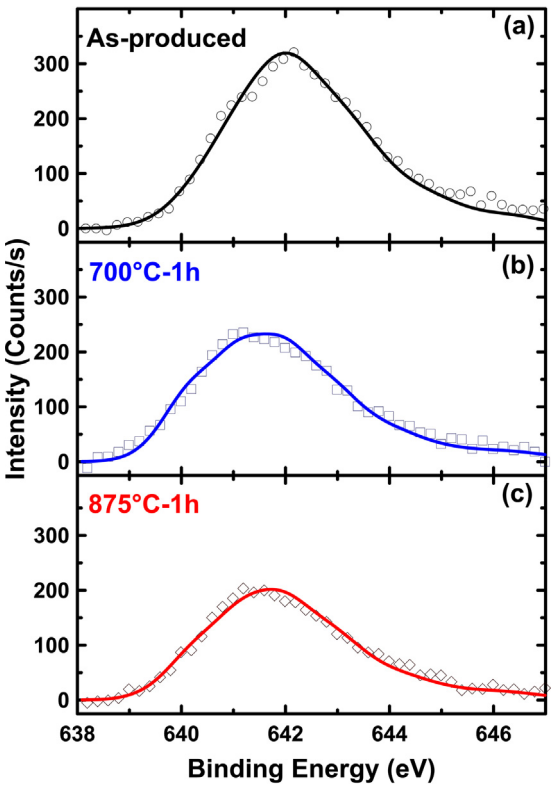

Fig. 6. XPS spectra of Mn 2p for the $Pt_{0.25}Mn_{0.75}$ alloy deposited on Vulcan carbon (a) As-produced and heat treated at (b) 700 °C and (c) 875 °C for 1 h in nitrogen atmosphere.

The XRD patterns obtained for Pt–Mn/C samples heat treated for different time periods are illustrated in Fig. 4a and b. The results showed that increasing the heat treatment time at 500 °C did not change the phases present. However, the intensification of the XRD peaks indicate that further crystallization has occurred. Only trace amounts of ordered phases were detected after 6 h of heat treatment at 500 °C. However, increasing the heat treatment time impacted the crystalline structure significantly at 700 °C (Fig. 4b). After 1 h of the heat treatment at 700 °C, the peaks for the Pt rich phase were still clearly observable (two closely-spaced peaks near 45°). However, when the sample was heat treated for more than one hour at 700 °C, the peaks associated with the Pt rich phase disappeared (e.g., the peak at 46.6°) and the PtMn ordered phase became prevalent. These results also agree with the TGA/DSC data which showed that the processes occurring at 700 °C requiring more time to complete.

PtMn/C alloy catalysts were analyzed by XPS before and after heat treatment in order to study any changes in their surface composition. The Pt 4f XPS spectra obtained for heat treated and untreated samples are shown in Fig. 5. The spectrum of Pt for treated and untreated samples were deconvoluted into two components, with asymmetric peak shapes. These signals are labeled as Pt0 and Pt1, which arise from zero-valent Pt and PtO, respectively [28–32]. The calculated relative percentages of each species, along with peak position and full width at half-maximum (FWHM) of Pt0 component are listed in Table 2.

The Mn 2p XPS spectra obtained for treated and untreated Pt–Mn/C samples are presented in Fig. 6. A broad spectrum was observed for Mn $2p_{3/2}$ emission, which indicates that Mn on the surface of the alloyed particles was oxidised and no Mn in metallic state was observable on the surfaces. The Mn oxide formation was also confirmed by the TGA analysis (Fig. 1a). Deconvolution of the Mn 2p spectrum revealed a complex mixture of several oxide compounds in multiple oxidation states [33–37]. Since these oxides are inactive towards EOR [9,38] and unstable in acidic solution [39], detailed study of these phases by XPS was not performed. However, the core Pt–Mn alloy phases formed and Mn within these alloys structures were indeed stable, as confirmed by prior electrochemical durability measurements [9,38]. XRD pattern obtained for a Pt–Mn alloy catalyst heat treated at 700 °C before and after immersion in 0.5 M H_2SO_4 for 24 h (Fig. S1) showed that the reflections associated with the alloy phase remain unchanged while the peaks associated with the oxide phases disappeared. This measurement confirms that the oxide layer was removed, revealing

Table 2
The binding energies, FWHM and species percentage of different Pt species as observed from the Pt (4f) X-ray photoelectron spectra of the heat treated and untreated Pt–Mn alloys.

Sample	Species relative intensity (%)		Pt $4f_{7/2}$ Peak position (eV)	Pt $4f_{7/2}$ Peak FWHM (eV)	Surface Atomic ratios of Mn versus Pt (%)
	Pt0	Pt1			
$Pt_{0.25}Mn_{0.75}$	90.6	9.4	71.18	1.20	84.98
$Pt_{0.25}Mn_{0.75}$-700 °C-1 h	95.7	4.3	71.11	0.88	82.44
$Pt_{0.25}Mn_{0.75}$-875 °C-1 h	96.7	3.3	71.20	1.08	86.76

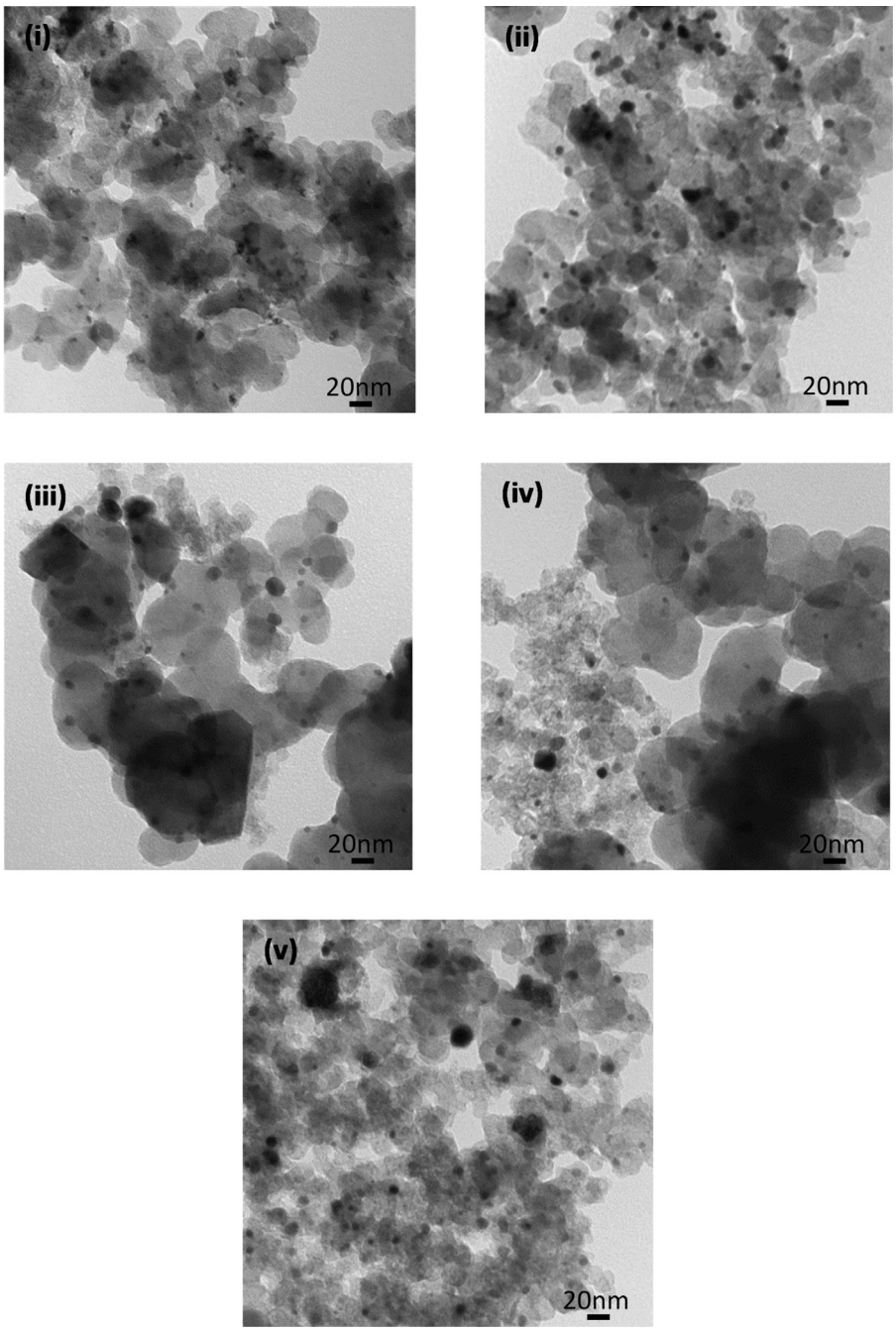

Fig. 7. TEM images of the Pt–Mn alloys before and after heat treatment in nitrogen atmosphere for constant period (1 h) at different temperatures (i) untreated (ii) 500, (iii) 700 (iv) 875 and (v) 950 °C.

the alloy phases at the surface for electrocatalysis. Similar behavior has been reported for Pt–Co alloy catalysts [40] where oxide phases and Co atoms on the surface of the nanoparticles dissolve resulting in a Pt skin surface which protects the alloyed particles from further corrosion and reduces the dissolution rate of the alloying element. We believe similar process has occurred for the Pt–Mn samples. Studies of the electrochemical durability the Pt–Mn alloys will be reported in the near future.

The binding energy for Pt0 and Pt1 (Fig. 5) in our samples are in good agreement with the literature for Pt/C catalysts [28]. The Pt0 peak position was shifted to higher binding energies compares to bulk Pt metal (71.2 eV versus 70.8 eV), which we have attributed to metal-support interaction and/or small cluster-size effects commonly observed in fuel cell catalysts [41]. The amount of Pt oxide content decreased with increasing heat treatment temperature. The atomic ratio of Mn on the surface was ~4 to ~9 at% higher than the bulk composition (Table 1). This indicates that some of the Mn migrated to the surface of the particles and formed a Mn oxide, leaving behind a more Pt-rich alloy core. Increasing the heat treatment temperature to 700 °C has marginally increased the Pt content on the surface which decreased again after the heat treatment at 875 °C.

After heat treatment at 700 °C, the Pt0 (Pt $4f_{7/2}$) peak to shifted to slightly more negative binding energies (~0.07 eV), and also became sharper (FWHM reduced by ~0.32 eV). These effects can be attributed to the particle size growth (reverse of small cluster-size effects) [42,43], which is inevitable during the heat treatment process. The negative shift could also be related to polarization

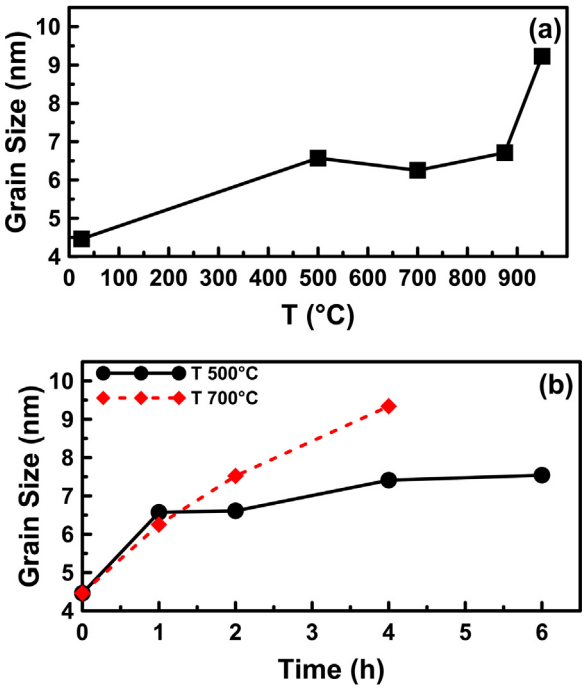

Fig. 8. The variation if average catalyst Pt–Mn particle size as a function of (a) temperature and (b) heat treatment time.

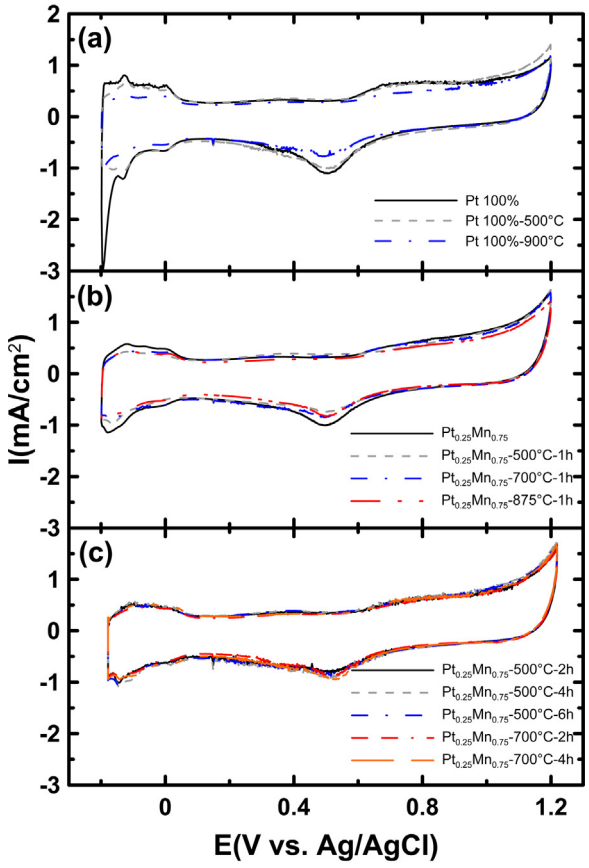

Fig. 9. CVs obtained for (a) Pt/C and (b) Pt–Mn/C catalysts before and after heat treatment for 1 h at different temperature. (c) CVs obtained for Pt–Mn/C catalysts heat treated for different time periods. Measurements were made in N_2-purged 0.5 M H_2SO_4 at a scan rate of 20 mV/s.

of the Pt–Mn bond or an electron withdrawing effect from the neighboring Mn atoms [28,43,44]. Further increasing the heat treatment temperature to 875 °C lead to phase separation had some effects on the electronic structure of nano particles. The Pt0 peak shifted to higher binding energies and also became slightly broader. Given the continuous particle size growth that occurred during heat treatment, the only reason for the positive shift is phase separation and the formation of a Pt rich phase (Pt_3Mn), which is in agreement with the XRD results.

TEM images of the as-synthesized samples and those heat treated at different temperatures are shown in Fig. 7. TEM images show that nano-sized catalyst particles were successfully produced. Furthermore, heat treatment resulted to an increase in particle sizes, including some very large particles with a diameter of more than 20 nm. Comparison of the TEM images acquired for untreated and treated samples revealed that particle agglomeration greatly contributed to the growth of very large particles during the heat treatment. Overall, the mean particle size was not substantially increased by heat treatment. Even at a heat treatment temperature of 950 °C, the average particle size was enlarged by only 5 nm. This shows that the alloyed particles were resistant to particle growth which has also been observed by others [45]. The particle sizes calculated from the TEM images are summarized in Table 3. Fig. 8a and b shows how the average particle size changed as a function of heat treatment temperature and heat treatment time at 500 and 700 °C. These results demonstrate that, although the chance of particle growth is greater at higher temperatures, the alloyed particles showed increased resistance to growth, even with a longer heat treatment period.

Based on the materials characterization data, the thermal evolution of the structure of the Pt–Mn alloy particles can be summarized as follow:

Table 3
Summary of electrochemical properties of the catalysts studied in this work.

	Half-wave potential (mV)	Peak potential (mV)	Peak current (mA/cm^2)	ECSA(m^2/g$_{Pt}$)	Mean particle size measured by TEM (nm)
Pt 100%	545	712	5.34	15.5	–
Pt100-500 °C-1 h	518	654	2.22	11.2	–
Pt100-900 °C-1 h	534	687	2.04	7.7	–
$Pt_{0.25}Mn_{0.75}$	497	665	2.49	10.5	4.46
$Pt_{0.25}Mn_{0.75}$-500 °C-1 h	520	650	2.02	5.1	6.57
$Pt_{0.25}Mn_{0.75}$-500 °C-2 h	542	686	3.26	7.6	6.61
$Pt_{0.25}Mn_{0.75}$-500 °C-4 h	538	694	3.00	8.1	7.41
$Pt_{0.25}Mn_{0.75}$-500 °C-6 h	548	699	3.17	7.0	7.54
$Pt_{0.25}Mn_{0.75}$-700 °C-1 h	544	682	2.60	6.6	6.25
$Pt_{0.25}Mn_{0.75}$-700 °C-2 h	545	712	5.34	8.1	7.52
$Pt_{0.25}Mn_{0.75}$-700 °C-4 h	537	699	6.49	8.7	9.34
$Pt_{0.25}Mn_{0.75}$-875 °C-1 h	473	697	3.58	7.9	6.71
$Pt_{0.25}Mn_{0.75}$-950 °C-1 h	475	715	2.88	8.4	9.23

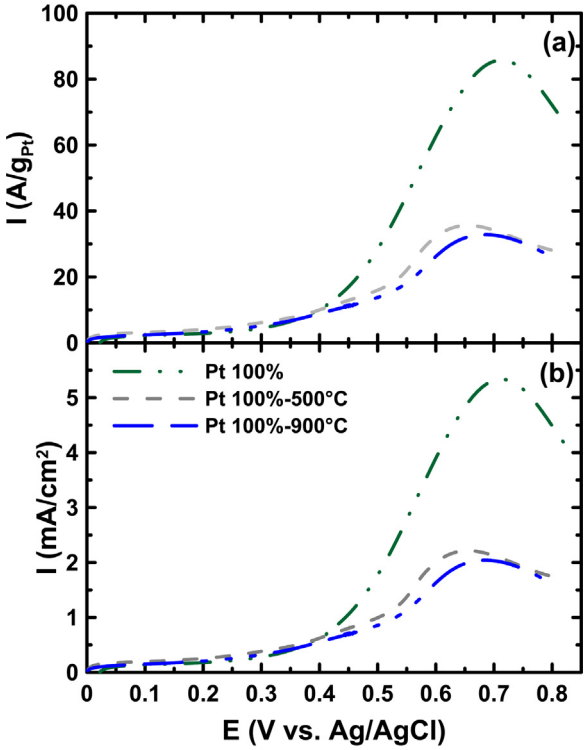

Fig. 10. LSVs obtained for pure Pt catalysts deposited on Vulcan carbon before and after heat treatment. The data is presented with the current normalized on the basis of (a) Pt content and (b) geometric area. Measurements were made in 0.5 M H_2SO_4 containing 0.1 M ethanol at a scan rate of 20 mV/s.

- The as-deposited $Pt_{0.25}Mn_{0.75}$/C catalysts contained a mixture of oxide phases and Pt–Mn alloy phases.
- Heat treatment at 500 °C intensified crystallization, but the Pt fcc structure was still predominant. The heat treatment period had almost no effect on the crystalline phase distribution at this temperature.
- At 700 °C, the Pt–Mn alloy phases were modified significantly. The ordered PtMn intermetallic phase was formed at this temperature. However, since the phase transformation was slow, the most predominant PtMn intermetallic alloy structure required longer heat treatment periods (4 h) to form.
- Increasing the heat treatment temperature to 875 °C led to phase separation, which created a mixture of the Pt_3Mn and PtMn intermetallic phases.
- All alloy particles had a layer of Mn-oxides present on the surface, which dissolved in acidic media to reveal the underlying Pt–Mn alloy core.

With a clear understanding of the alloy particle composition and morphology for each catalyst, a clear relationship between their structure and electrochemical properties can be more readily made.

3.2. Electrochemical characterization

Electrochemical studies in a deaerated 0.5 M H_2SO_4 solution were conducted on the samples before and after heat treatment and the results are presented in Fig. 9. All samples showed the common Pt CV shape. The presence of clearly resolved hydrogen adsorption/desorption peaks at low potential indicates that any surface manganese oxide layer was been removed, revealing the Pt-alloy surface. The ECSA values were calculated by integrating the charge under the hydrogen adsorption peaks and are compiled in Table 3. The results show that the ECSA values for pure Pt/C dramatically and continuously decreased from 15.5 to 7.7 m^2/g_{Pt} by treating samples at 500 and 900 °C. However, ECSA values of Pt–Mn/C samples behaved quite differently. After heat treatment at 500 °C, the ECSA values for Pt–Mn samples were reduced by ca. 50%, but the ECSA for the alloyed samples improved after increasing the heat treatment temperature above 700 °C. A similar trend was also observed by increasing the heat treatment time. Particle size

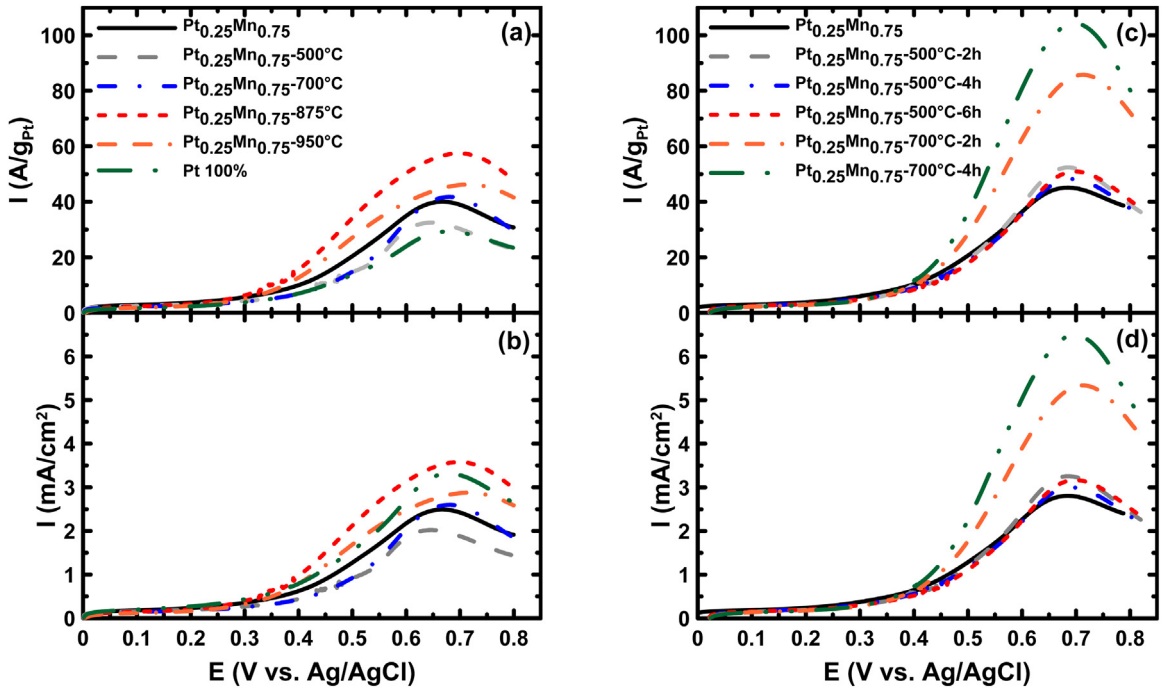

Fig. 11. LSVs obtained for Pt–Mn alloys deposited on Vulcan carbon before and after heat treatment at (a and b) different temperatures for 1 h and (c and d) different temperatures for 2–6 h. The data is presented with the current normalized on the basis of (a and c) Pt content and (b and d) geometric area. Measurements were made in 0.5 M H_2SO_4 containing 0.1 M ethanol at a scan rate of 20 mV/s.

growth is one of the main reasons for the drop in ECSA for all heat treated catalysts, both alloy and pure metal. However, the optimal heat treatment process for the Pt–Mn alloy led to an ECSA that was only 20% lower than that of the untreated sample. This resistance to ECSA loss is most likely due to a roughening of the alloy particle surface upon dissolution of the surface oxide layer [39,40,46,47].

The EOR activity of the pure Pt samples, before and after heat treatment, is displayed in Fig. 10. Comparing the peak current density of the heat treated samples with the as-produced sample showed that the electrochemical activity continuously decreased by increasing the treatment temperature (Table 3). This loss in activity can be attributed to the substantial growth in Pt particle size upon heat treatment.

The EOR activity of the Pt–Mn/C catalysts, before and after heat treatment, is shown in Fig. 11a and b. Heat treatment at 500 °C led to a decrease in catalytic activity. This was not surprising since at 500 °C no new phases were formed and the particle size increased. Upon increasing the heat treatment temperature, EOR activity began to improve and at 875 °C EOR activity surpassed that of the untreated sample pure Pt sample. Upon raising the heat treatment temperature to 950 °C, EOR activity decreased slightly, though it was still higher than that achieved with the untreated sample.

To compare the data based on the Pt content, the EOR activity is plotted using Pt-mass specific current in Fig. 11a. These plots show that the sample heat treated at 875 °C had about double the mass-activity (measured by peak current) of the pure Pt catalysts. In addition, the most active alloys showed a lower half-wave potential for EOR. This, coupled with the lower ECSA compared to the untreated catalyst, indicates that there is an electronic effect associated with the increased EOR activity of the annealed Pt–Mn/C catalysts, which we have attributed to the presence of the intermetallic alloy phase.

The impact of heat treatment time at 500 °C and 700 °C are shown in Fig. 11d. Increasing the heat treatment time beyond 2 h at 500 °C had no impact on EOR activity. This is in agreement with our XRD and TGA data that indicated only a minimal structural changes at this temperature. However, increasing the treatment period at 700 °C up to 4 h improved the activity continuously, leading to a two-fold increase in peak EOR current and a decrease in the half-wave potential for the EOR. This increased activity parallels the phase transformations that occurred at 700 °C as a function of heat treatment time. Longer heat treatment times at 700 °C produces more of the PtMn intermetallic alloy, which was responsible for the improved EOR activity.

Finally, electrochemical and material characterization confirm that, although different metal deposition rates lead to inhomogeneous alloys during chemical deposition, optimized heat treatment conditions have improved homogeneity and the EOR activity of the catalysts. Furthermore, a specific heat treatment cycle can result in the most active crystalline structures, which enhance the EOR activity.

4. Conclusion

In this work, Pt and Pt–Mn alloys were synthesized and the effect of both heat treatment temperature and time on the structure and electrochemical properties of Pt–Mn/C alloy catalysts were investigated. The as-deposited Pt–Mn/C catalysts contained a mixture of alloy and oxide. DSC measurements showed that several phase transitions occurred between 500 °C and 900 °C and most of these transitions are endothermic. XRD analysis indicated that the PtMn intermetallic was formed at 700 °C, and that this phase transitions required about 4 h at that temperature to completely form. Heat treatment at 875 °C resulted in the formation of a mixture of PtMn and Pt_3Mn intermetallic phases. TEM analysis indicated that alloyed particles showed resistance to particle growth. By examining EOR activity for catalysts prepared at different heat treatment temperatures, we have determined that the most active phase for EOR is the PtMn intermetallic phase. Maximum EOR activity occurred when the samples were heat treated at 700 °C for 4 h, which corresponded to the highest concentration of this PtMn intermetallic phase with a relatively small loss in ECSA compared to the as-produced samples.

Acknowledgements

This work was supported by the Natural Sciences and Engineering Research Council (NSERC) of Canada, Alcohol Countermeasure Systems Corp., and UOIT. The authors also acknowledge equipment support from the Canada Foundation for Innovation. We thank Wen He Gong (McMaster University) for the XRD data, Dr. Richard B. Gardiner (University of Western Ontario) for the TEM images and Dr. Mark Biesinger (Surface Science Western, University of Western Ontario) for XPS analysis.

Appendix A. Supplementary data

Supplementary data associated with this article can be found, in the online version, at http://dx.doi.org/10.1016/j.apcatb.2015.03.051.

References

[1] E. Antolini, Mater. Chem. Phys. 78 (3) (2003) 563–573.
[2] A. Rabis, P. Rodrigue, T.J. Schmidt, ACS Catal. 2 (5) (2012) 864–890.
[3] H. Liu, C. Songa, L. Zhang, J. Zhang, H. Wang, D.P. Wilkinson, J. Power Sources 155 (2006) 95–110.
[4] T. Ghosh, B.M. Leonard, Q. Zhou, F.J. DiSalvo, Chem. Mater. 22 (7) (2010) 2190–2202.
[5] W. Vielstich, A. Lamm, H.A. Gasteiger, Handbook of Fuel Cells: Fundamental, Technology, and Applications, Wiley, 2003.
[6] F. Vigier, S. Rousseau, C. Coutanceau, J. Leger, C. Lamy, Top. Catal. 40 (1–4) (2006) 111–121.
[7] T. Sato, K. Okaya, K. Kunimatsu, H. Yano, M. Watanabe, H. Uchida, ACS Catal. 2 (3) (2012) 450–455.
[8] E. Antolini, J.R.C. Salgado, E.R. Gonzalez, Appl. Catal. B 63 (1–2) (2006) 137–149.
[9] M. Ammam, E.B. Easton, J. Electrochem. Soc. 159 (5) (2012) B635–B640.
[10] M. Ammam, E.B. Easton, J. Power Sources 215 (0) (2012) 188–198.
[11] W. Roh, J. Cho, H. Kim, J. AppL. Electrochem. 26 (6) (1996) 623–630.
[12] T.J. Schmidt, H.A. Gasteiger, R.J. Behm, Electrochem. Commun. 1 (1) (1999) 1–4.
[13] H. Li, G. Sun, L. Cao, L. Jiang, Q. Xin, Electrochim. Acta 52 (24) (2007) 6622–6629.
[14] F. Vigier, C. Coutanceau, A. Perrard, E.M. Belgsir, C. Lamy, J. Appl. Electrochem. 34 (4) (2004) 439–446.
[15] T.S. Almeida, L.M. Palma, C. Morais, K.B. Kokoh, A.R. De Andrade, J. Electrochem. Soc. 160 (9) (2013) F965–F971.
[16] E. Antolini, F. Colmati, E.R. Gonzalez, Electrochem. Commun. 9 (3) (2007) 398–404.
[17] Q. He, S. Mukerjee, Electrochim. Acta 55 (5) (2010) 1709–1719.
[18] C. Lamy, S. Rousseau, E.M. Belgsir, C. Coutanceau, J.M. Léger, Electrochim. Acta 49 (22–23) (2004) 3901–3908.
[19] E. Antolinia, E.R. Gonzalez, Catal. Today 160 (2011) 28–38.
[20] S. Liao, K.A. Holmes, H. Tsaprailis, V.I. Birss, J. Am. Chem. Soc. 128 (11) (2006) 3504–3505.
[21] C.W.B. Bezerra, L. Zhang, H. Liu, K. Lee, A.a.L.B. Marques, E.P. Marques, H. Wang, J. Zhang, J. Power Sources 173 (2) (2007) 891–908.
[22] J.A. Wittkopf, J. Zheng, Y. Yan, ACS Catal. 4 (9) (2014) 3145–3151.
[23] B.C. Beard, P.N. Ross, J. Electrochem. Soc. 137 (11) (1990) 3368–3374.
[24] M. Ammam, L.E. Prest, A.D. Pauric, E.B. Easton, J. Electrochem. Soc. 159 (2) (2012) B195–B200.
[25] K.H. Kangasniemi, D.A. Condit, T.D. Jarvi, J. Electrochem. Soc. 151 (4) (2004) E125–E132.
[26] O.A. Baturina, S.R. Aubuchon, K.J. Wynne, Chem. Mater. 18 (6) (2006) 1498–1504.
[27] E.R. Stobbe, B.A. de Boer, J.W. Geus, Catal. Today 47 (1–4) (1999) 161–167.
[28] A.K. Shukla, M. Neergat, P. Bera, V. Jayaram, M.S. Hegde, J. Electroanal. Chem. 504 (1) (2001) 111–119.
[29] A.S. Aricò, A.K. Shukla, H. Kim, S. Park, M. Min, V. Antonucci, Appl. Surf. Sci. 172 (1–2) (2001) 33–40.

[30] Y. Ma, H. Wang, S. Ji, V. Linkov, R. Wang, J. Power Sources 247 (0) (2014) 142–150.
[31] J. Zeng, J.Y. Lee, J. Power Sources 140 (2) (2005) 268–273.
[32] Z.Q. Tian, S.P. Jiang, Y.M. Liang, P.K. Shen, J. Phys. Chem. B 110 (11) (2006) 5343–5350.
[33] M.C. Biesinger, B.P. Payne, A.P. Grosvenor, L.W.M. Lau, A.R. Gerson, R.S. Smart, Appl. Surf. Sci. 257 (7) (2011) 2717–2730.
[34] R.J. Iwanowski, M.H. Heinonen, W. Paszkowicz, R. Minikaev, T. Story, B. Witkowska, Appl. Surf. Sci. 252 (10) (2006) 3632–3641.
[35] H.W. Nesbitt, D. Banerjee, Am. Mineral. 83 (3–4) (1998) 305–315.
[36] Q.H. Wu, M. Liu, W. Jaegermann, Mater. Lett. 59 (16) (2005) 1980–1983.
[37] A.A. Mirzaei, H.R. Shaterian, M. Kaykhaii, Appl. Surf. Sci. 239 (2) (2005) 246–254.
[38] M. Ammam, E.B. Easton, J. Power Sources 236 (2013) 311–320.
[39] J.E. Harlow, D.A. Stevens, R.J. Sanderson, G.C.K. Liu, L.B. Lohstreter, G.D. Vernstrom, R.T. Atanasoski, M.K. Debe, J.R. Dahn, J. Electrochem. Soc. 159 (6) (2012) B670–B676.
[40] M. Watanabe, K. Tsurumi, T. Mizukami, T. Nakamura, P. Stonehart, J. Electrochem. Soc. 141 (10) (1994) 2659–2668.
[41] A.K. Shukla, M.K. Ravikumar, A. Roy, S.R. Barman, D.D. Sarma, A.S. Aricò, V. Antonucci, L. Pino, N. Giordano, J. Electrochem. Soc. 141 (6) (1994) 1517–1522.
[42] W.P. Zhou, A. Lewera, R. Larsen, R.I. Masel, P.S. Bagus, A. Wieckowski, J. Phys. Chem. B 110 (27) (2006) 13393–13398.
[43] R.J. Isaifan, S. Ntais, E.A. Baranova, Appl. Catal. A. General 464–465 (0) (2013) 87–94.
[44] K.W. Park, J.H. Choi, Y.E. Sung, J. Phys. Chem. B 107 (24) (2003) 5851–5856.
[45] E. Antolini, J. Mater. Sci. 38 (14) (2003) 2995–3005.
[46] D.A. Stevens, R. Mehrotra, R.J. Sanderson, G.D. Vernstrom, R.T. Atanasoski, M.K. Debe, J.R. Dahn, J. Electrochem. Soc. 158 (8) (2011) B905–B909.
[47] C. Chen, Y. Kang, Z. Huo, Z. Zhu, W. Huang, H.L. Xin, J.D. Snyder, D. Li, J.A. Herron, M. Mavrikakis, M. Chi, K.L. More, Y. Li, N.M. Markovic, G.A. Somorjai, P. Yang, V.R. Stamenkovic, Science 343 (6177) (2015) 1339–1343.